Effects of jet-injection-pipe length on the flow-control effectiveness of spanwise-inclined jets in supersonic crossflow

Deepak Prem Ramaswamy ⊙,* Robin Sebastian ⊙, and Anne-Marie Schreyer ⊙

Chair of Fluid Mechanics and Institute of Aerodynamics, RWTH Aachen University, 52062 Aachen, Germany

Jets-in-supersonic-crossflow have many influential areas of technical applications, amongst them the field of separation control when implemented as air-jet vortex generators (AJVGs). The jet velocity profile at the exit of the jet orifice is affected by the jet-injection-pipe length. In this study, we utilize a combined experimental-numerical approach to characterize the effect of jet-velocity profile on the jet-induced structures and their direct impact on AJVG separation-control effectiveness. First, we conducted large-eddy simulations (LESs) of two single spanwise-inclined jet-in-crossflow configurations with different injection-pipe lengths. The case with a short jet-pipe length exhibits an underdeveloped flow in the pipe with unstable growth modes. The longer jet-pipe length, on the other hand, allows for a fully established velocity profile and contributes to stronger and more coherent jet-induced structures. Equipped with this knowledge, we conducted detailed experiments applying AJVGs with both pipe lengths to control shock-induced flow separation and assessing the respective control effectiveness. The experiments were conducted at similar crossflow and jet-plenum conditions as the LESs for both jet-pipe lengths. The control effectiveness of longer-pipe jets is higher, with a 24% reduction in flow-separation length compared with only 17% reduction for the shorter-pipe case with underdeveloped jet flow. Boundary-layer velocity measurements downstream of the jets show the expected higher velocities close to the wall for the longer-pipe case, which are related to the stronger jet-induced streamwise vortices that are responsible for the improved control effectiveness.

I. INTRODUCTION

The interaction between a shock wave and a boundary layer is a prevalent yet unfavorable flow phenomenon in many high-speed aerospace applications. Such interactions can lead to a large-scale separation of the flow if the incoming boundary layer experiences a strong adverse pressure gradient as it encounters the shock wave [1]. A salient feature of such shock-induced flow separations is the occurrence of low-frequency oscillations of the shock/separation-bubble system [2]. These unsteady flow separations are undesirable and can jeopardize the safe and reliable operation of the vehicle by causing fluctuating pressure and thermal loads on the surface, material fatigue, and failure due to resonance, etc. [3]. Therefore, the research community has been actively studying both the general characteristics of these interactions and strategies to inhibit them [1–6].

Flow separation primarily culminates due to the presence of the low-momentum fluid close to the wall [7]. Therefore, a common strategy to avert separation is to bleed away this region, which has been shown to successfully subdue shock-induced separations (see, e.g., Harloff and Smith [8]). However, this strategy suffers from the expulsion of valuable mass-flow rate, which, in the

---

*d.ramaswamy@aia.rwth-aachen.de

context of supersonic engine inlets, results in loss of thrust. A superior technique to improve the boundary layer's ability to resist flow separation is to redistribute its momentum by bringing higher-momentum fluid from the upper part of the boundary layer close to the wall. Such a redistribution can be readily achieved by the introduction of streamwise vortices into the boundary layer [4,5,9,10].

A number of active and passive techniques to generate streamwise vortices in order to mitigate separation have been studied in literature. Traditionally, protuberances in the boundary layer, such as ramps, vanes, cylinders, etc., were used to redirect the incoming crossflow and generate streamwise vortices downstream of their installation [5]. Such mechanical vortex generators, while effective, are designed for specific flow conditions that prevail only during parts of the flight trajectory and exhibit sustained parasitic drag under all flow conditions. Therefore, to circumvent these drawbacks, air-jet vortex generators were adopted [10]. When air jets are injected onto the incoming crossflow, the resulting jet-in-crossflow interaction ensures the generation of counter-rotating vortex pairs (CVPs) [11,12], similarly to those from mechanical vortex generators. As a result, the separation-control effectiveness of such air-jet vortex generators is comparable to that of mechanical vortex generators [4]. However, the effectiveness depends on a number of geometrical and flow parameters.

The separation-control effectiveness for given flow conditions can be improved by optimizing the various air-jet geometric parameters, with the aim to achieve a sustained streamwise vorticity with an aversion to early jet lift-off. Early experiments [4,10,13] have pointed out that a spanwise-inclined configuration of jet injection improves the control effectiveness in comparison to their wall-normal counterparts. With the advent of high-performance computing, it became possible to analyze the physics of jets-in-supersonic-crossflow in detail. Sebastian *et al.* [12] investigated the flow structures induced by a spanwise-inclined single jet injected into a supersonic crossflow using large-eddy simulations (LESs) and concluded that the improved control effectiveness can be attributed to stronger and asymmetrical counter-rotating streamwise vortices that sustain for a longer downstream distance without lift off. Studies have also shown that stronger streamwise vortices, and thereby an improved control effectiveness, can also be induced by varying the jet-orifice diameter d_{jet} [14,15] and/or shape [16–18].

Furthermore, several experimental [19–21] and numerical [16,22] results have highlighted the need to achieve an optimal degree of interaction between adjacent jets in a control array to ensure good control effectiveness. A direct approach to accomplish this is by adapting the spacing between the jets in the array. For jet spacing between $7d_{\mathrm{jet}} - 13d_{\mathrm{jet}}$, the jet-induced vortices constructively interfere with respective neighboring vortices and thereby enhance the streamwise vorticity due to an improved momentum transfer. This effect improves the boundary layer's ability to resist flow separation [16,19–21]. A favorable interaction between the jets in the array can also be brought about by controlling the jet-injection pressure; these two parameters show an interplay in defining the intensity of jet/jet interactions [19,22].

For a more comprehensive understanding of the flow-structures induced by air-jet vortex generators, jet-in-supersonic-crossflow (JISCF) literature can be beneficial (see Mahesh [23] for an overview). However, a vast majority of these studies target air/fuel injections or film-cooling applications and therefore employ $d_{\mathrm{jet}} = O(\delta)$ (δ is the boundary-layer thickness), whereas jets for control applications are typically $d_{\mathrm{jet}} \leqslant 0.25\delta$ (following Szwaba [14]). The larger diameter causes the jet-induced structures to penetrate beyond the boundary layer and thus increase parasitic drag; such configurations are therefore undesirable for separation-control applications [14]. Sebastian *et al.* [12] performed the only study (to the authors' knowledge) of flow-structures downstream of a single spanwise-inclined jet-in-supersonic-crossflow, and in particular of a jet with $d_{\mathrm{jet}} \leqslant 0.25\delta$. They observed the formation of complex and distinctly asymmetric vortical structures. While the jet-induced structures are favorable for separation-control purposes, the authors also reported the presence of an underdeveloped jet flow in the investigated pipe geometry, with inflection points in the velocity profiles, which can lead to instabilities.

Experiments on JISCF generally lack the spatial resolution to report on the jet-pipe flow. Therefore, sonic jet-exit conditions are usually presumed on the basis of an assumption of inviscid flow in the pipe [20,21,24–27]. On the other hand, past numerical studies on JISCF imposed jet

flow either using a uniform velocity profile with sonic exit conditions [28,29] or, alternatively, a nozzle-chamber/pipe with a pressure-inlet condition [30–33]; they offer incomplete discussions on the nature of the jet-pipe flow and its effects on the jet-induced structures in the crossflow. Imposing such boundary conditions for the jet-flow is simpler and reduces computational costs, which helps explain its wide implementation in literature. To be able to accurately capture the physics of the jet flow and to match the experimental conditions of Ramaswamy and Schreyer [34], Sebastian *et al.* [12] used a computational domain consisting of (a) a plenum with a constant-pressure boundary condition, (b) a pipe connecting the plenum and the crossflow, and (c) a Mach 2.5 flat-plate turbulent boundary layer into which the jet is injected. To the authors' knowledge, similar plenum/pipe configurations are not available in literature, possibly owing to the increase in computational complexity. Consequently, literature on JISCF usually lacks insights on the evolution and influence of the flow within the jet pipe, especially with changing pipe length.

Studies on subsonic jets injected into subsonic crossflow have highlighted a direct influence of the jet-exit velocity profile on the jet-induced structures, as well as their penetration behavior into the crossflow [35–38]; similar studies employing a sonic/supersonic jet of varying jet-velocity profiles injected into a supersonic crossflow are lacking so far. Any potential changes in the JISCF characteristics due to the nature of the jet-pipe flow will, however, directly influence the jet-induced counter-rotating vortices and consequently the separation-control effectiveness, when the jets are implemented in an air-jet vortex generator (AJVG) control configuration.

In the present study, we therefore investigate the effects of differences in the jet-pipe flow on the JISCF topology, as well as on the AJVG control effectiveness for the first time. For this, we undertake a combined experimental-numerical effort: We carry out a LES of a single spanwise-inclined jet-in-supersonic-crossflow for the same conditions as in Sebastian *et al.* [12] but with a fully developed jet-pipe flow. This was achieved by increasing the length of the jet-injection pipe. Furthermore, we perform experiments to evaluate the separation-control effectiveness of such jets when implemented in an AJVG-control array installed upstream of a 24° compression-ramp-induced shock-wave/boundary-layer interaction. Both the experimental and numerical analyses are conducted for the same geometrical and crossflow conditions. This combined approach helps circumvent any disadvantages inherent to purely numerical (computational costs, data storage, etc.) or experimental studies (insufficient spatial and temporal resolution of the jet flow, etc.).

The manuscript is structured as follows. The numerical method and computational framework for the single-JISCF LES will be discussed in Sec. II. The flow facility and experimental/measurement setup will be introduced in Sec. III. The results include a validation of the boundary-layer statistics (Sec. IV A) and comparisons of single-jet pipe flow and JISCF characteristics for two different pipe lengths in Secs. IV C and IV D, respectively. These findings will then be utilized to help interpret the experimental results on separation-control effectiveness in Sec. IV E. Finally, the main findings are summarized in Sec. V.

II. COMPUTATIONAL FRAMEWORK

A. Numerical methods

Numerical simulations of the single spanwise-inclined jet in supersonic crossflow were carried out using the efficient in-house multiphysics solver m-AIA (previously referred to as ZFS) [39]. The unsteady compressible Navier-Stokes equations are solved using a finite volume method on a block-structured mesh. The convective and diffusive fluxes are discretized using a second-order-accurate advection upstream splitting method (AUSM) [40] and a modified cell-vertex scheme [41], respectively. The monotone upstream scheme for conservation laws with the Venkatakrishnan limiter [42] is used to reconstruct the cell surface values and to prevent nonphysical oscillations by steep and strong shocks. The time integration is carried out by a five-stage Runge-Kutta method at second-order accuracy.

To perform the LESs, we used the monotonically integrated LES approach, where the dissipation of the turbulence spectrum at high wave numbers is mimicked by the AUSM scheme's numerical
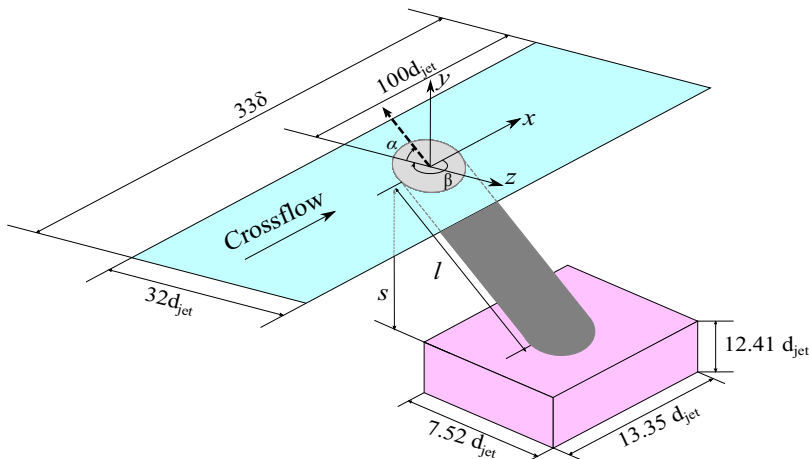
FIG. 1. Schematic representation of the computational domain for the single JISCF-LES.

dissipation [43]. Meinke *et al.* [41] discussed the influence of the order of the method and the subgrid-scale model on the overall accuracy of the solution in detail. Meinke *et al.* [41] have also shown that the AUSM scheme without a subgrid scale model is a suitable and reliable method to capture turbulence and that the subgrid models increase the dissipation and damp the small-scale structures. Furthermore, we ensured that the energy-containing turbulent motions are captured accurately by performing a grid sensitivity study (see Sec. II B). The numerical method has been validated and shown to be appropriate for the present case by computing turbulent boundary layers [44], shock-wave/boundary-layer interactions (SWBLIs) [45,46], jets of different configurations in supersonic crossflow [22,47–49], as well as separation control with an array of air-jet vortex generators [50].

Unless specified otherwise, the following nondimensionalization is used for the velocity $\mathbf{u} = \tilde{\mathbf{u}}/\tilde{a}_0$, where the speed of sound is $\tilde{a}_0 = \sqrt{\gamma \tilde{P}_0/\tilde{\rho}_0}$, γ is the ratio of specific heats, and $\tilde{\cdot}$ denotes dimensional quantities. Temperature, density, and pressure are nondimensionalized as $T = \tilde{T}/\tilde{T}_0$, $\rho = \tilde{\rho}/\tilde{\rho}_0$, and $P = \tilde{P}/\tilde{\rho}_0\tilde{a}_0^2$, respectively; the viscosity μ is expressed using Sutherland's law. Spatial dimensions are nondimensionalized using the jet-injection-pipe diameter d_{jet}: $\mathbf{x} = \tilde{\mathbf{x}}/\tilde{d}_{\text{jet}}$. Time-averaged quantities are denoted with $< \cdot >$, time- and spanwise-averaged quantities with $\overline{\cdot}$, and fluctuating quantities with superscript $'$.

We use the following subscripts: "0" marks values at stagnation conditions, "∞" denotes freestream values, "w" is used for values at the flat-plate surface, "ax" for values along the pipe length axis, "δ" for values at the boundary-layer edge. "θ" and "τ" refer to quantities based on the momentum thickness and wall shear stress. "x," "y," "z" indicate streamwise, wall-normal, and spanwise quantities, respectively. As superscripts, we use "+" for values in viscous units, "vd" for van Driest scaled quantities, "j" for values close to the jet exit.

B. Computational setup

The computational setup of the current simulation is similar to that of Sebastian *et al.* [12]. It consists of three subdomains: (i) a pressure plenum, (ii) a Mach 2.5 flat-plate turbulent boundary layer, and (iii) a spanwise-inclined circular jet-injection pipe connecting the plenum and the crossflow subdomains (see schematic shown in Fig. 1). The supersonic crossflow is characterized by a freestream Mach number $M_\infty = 2.5$ and momentum-thickness based Reynolds number $\text{Re}_\theta = 7000$. The origin (O)(0, 0, 0) of the coordinate system is at the jet-injection location on the flat-plate surface. To capture the far-field effects of jet injection, we considered a long downstream extent of

TABLE I. LES crossflow parameters.

M_∞	Re_θ	P_o	T_o	δ	u_∞
2.5	7000	101.325 kPa	295 K	9.4×10^{-3} m	578 m/s

the crossflow subdomain $\sim 100 d_{\mathrm{jet}}$. A summary of the main cross-flow parameters is available in Table I.

The circular pipe connecting the plenum and the flat-plate surface has a diameter of $d_{\mathrm{jet}} = 1$ mm, where $\delta/d_{\mathrm{jet}} \approx 10$. The pipe is spanwise inclined at an angle of $\alpha = 45°$ (in the y-z plane) and $\beta = -90°$ (in the x-z plane) with respect to the x axis. The flow in the pipe is fed via the pressure plenum located beneath the flat-plate surface. Sebastian $et\ al.$ [12] utilized a pipe length of $l = 4.24 d_{\mathrm{jet}}$ by placing the plenum $s = 3 d_{\mathrm{jet}}$ below the flat-plate surface (case SP). We modified the setup by placing the pressure plenum $s = 13 d_{\mathrm{jet}}$ below the flat-plate surface, thereby creating a longer jet-pipe length of $l = 18.38 d_{\mathrm{jet}}$ (case LP). The main jet parameters at the pipe exit are summarized in Table II. Further details on the geometry, computational grid, numerical scheme, simulation setup, and boundary conditions can be found in Sebastian $et\ al.$ [12], where LESs were performed under identical conditions, except for the jet-pipe length (l). We performed a systematic analysis of grid sensitivity in Refs. [12,16] by comparing the numerical results of the incoming boundary layer with the boundary layer in an experiment [34] at comparable conditions and a reference DNS data of an incompressible turbulent boundary layer at $\mathrm{Re}_\theta = 2540$ by Schlatter and Örlü [51]. A mesh resolution of $\Delta x^+ = 10$, $\Delta y_w{}^+ = 1$, $\Delta y_{\delta_{99}}^+ = 12$, and $\Delta z^+ = 5$ was found suitable for the present case with an uncertainty of approximately 1.1% on the u_τ estimation with respect to the companion experimental study [12,47]. In the vicinity of the jet-injection location, additional local refinement of the mesh was carried out to accurately capture the flow physics (see Refs. [12,16] for further details).

The obtained results were time-averaged to analyze the evolution of the mean flow topology. The vortical structures were identified using the Q criterion technique [52]. Furthermore, we performed a dynamic mode decomposition (DMD) [53,54] of the time-resolved sequence of the pipe flow to extract spatial representations of dynamically relevant modes and their characteristic frequencies. The sparsity-promoting algorithm of Jovanović $et\ al.$ [55] was used to directly select the most relevant modes.

III. EXPERIMENTAL SETUP

In addition to the LESs of spanwise-inclined single JISCF, we performed experiments studying arrays of spanwise-inclined jets in supersonic crossflow, resulting in an AJVG configuration that is commonly used to control shock-induced flow separations [14,19–21,26,34,56]. This section provides details on the experimental setup and AJVG configuration.

A. Flow-facility and compression-ramp model

Our experiments were conducted in the trisonic wind-tunnel facility at the Institute of Aerodynamics, RWTH Aachen University. The in-draft facility is driven by a large 4×95 m^3 vacuum tank

TABLE II. Jet-flow parameters.

Case	Pipe-length (l)	APR $\left(P_{\mathrm{oj}}^{\mathrm{pl}}/P_o\right)$	P_j	ρ_j	u_j	J
SP [12]	$4.24 d_{\mathrm{jet}}$	1	$9.30\ P_\infty$	$3.18 \rho_\infty$	$0.900 u_\infty$	1.52
LP	$18.38 d_{\mathrm{jet}}$	1	$7.96\ P_\infty$	$2.67 \rho_\infty$	$0.965 u_\infty$	1.45

TABLE III. Experimental conditions.

M_∞	u_∞	Re_∞	P_o	T_o
$2.52 \pm 0.6\%$	581.2 m/s	9.6×10^6 m^{-1} $\pm 2.8\%$	99.49 kPa $\pm1.42\%$	297 K $\pm1.15\%$

and is supplied with dry air from a large 165 m^3 reservoir balloon. Therefore, the ambient conditions in the laboratory define the stagnation conditions of the flow facility. The freestream Mach number is set by operating a variable throat, and for a selected Mach number of $M_\infty = 2.52$, a freestream unit Reynolds number of $\mathrm{Re}_\infty = 9.62 \times 10^6$ m^{-1} ensues in the test section. Optical access for the 400 mm $\times$ 400 mm test section is available via two quartz windows on each side and a third window on the top wall. The freestream conditions are chosen to match the LES simulations from Sec. II and are summarized in Table III.

A strongly separated shock-wave/turbulent-boundary-layer interaction was generated with a 24° compression-ramp model installed on a flat plate [see Fig. 2(a)]. The flat plate spans the entire width of the test section. The 24° 2D ramp section was installed at 69.42δ downstream of the flat-plate leading edge. A zig-zag trip installed at $\sim 1\delta$ downstream of the flat-plate leading edge ensured a homogeneous turbulent boundary layer close to the measurement region. The turbulent boundary layer was characterized in Ramaswamy and Schreyer [34] and measured to be $\delta = 10.4$ mm at $x = -4.5\delta$ upstream of the ramp corner, with $\mathrm{Re}_\theta = 8225$.

At 7.69δ upstream of the ramp corner, a modular AJVG array was installed. It consists of a spanwise series of 23 circular orifices of $d_{\mathrm{jet}} = 0.1\delta$. As in the LES setup, the jets are spanwise inclined, with a pitch angle of $\alpha = 45°$ with respect to the plate surface and a skew angle of $\beta = -90°$ with respect to the streamwise direction [see schematic in Fig. 2(b)]. Air jets are injected via the circular orifices by means of a pressure plenum placed within the flat-plate model. The total pressure in the plenum ($P_{\mathrm{oj}}^{\mathrm{pl}}$) was set to be equal to the crossflow stagnation pressure (P_o), i.e., $P_{\mathrm{oj}}^{\mathrm{pl}}/P_o = \mathrm{APR} = 1$. The spanwise jet-to-jet spacing is $D = 8d_{\mathrm{jet}}$, which results in favorable interactions between the jets in the array [20,22] for the selected jet-injection pressure.

As in the LESs, two different jet-pipe lengths were tested—a jet-pipe length of $4.24d_{\mathrm{jet}}$ [short-pipe (SP) AJVG array] and a second longer jet-pipe length of $18.38d_{\mathrm{jet}}$ [long-pipe (LP) AJVG array]. All further jet and crossflow parameters remain identical for both cases. Table IV provides a summary of some of the main AJVG geometrical and flow parameters. The origin of the coordinate system is at the jet-injection location, along the model centerline. For further details on the flow facility, wind-tunnel model, and AJVG setup, the reader is referred to Ramaswamy and Schreyer [20,34].
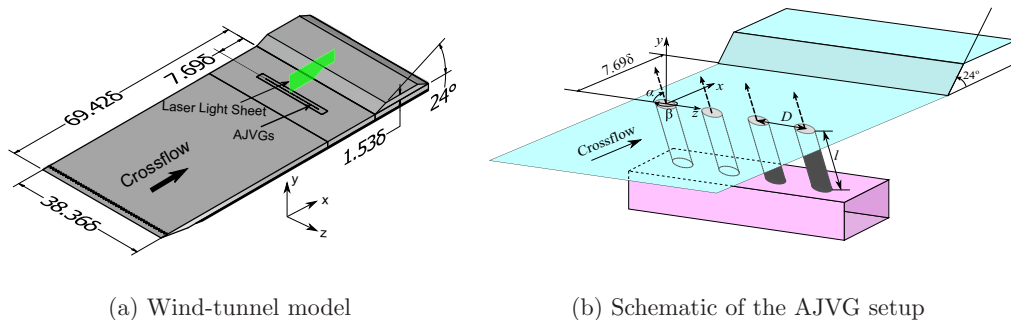

(a) Wind-tunnel model   (b) Schematic of the AJVG setup

FIG. 2. Experimental setup to test the flow-control effectiveness of the jet configurations.

TABLE IV. AJVG geometrical parameters.

	Case	
Parameters	SP	LP [34]
Jet-pipe length (l)	$4.24d_{\mathrm{jet}}$	$18.38d_{\mathrm{jet}}$
Orifice diameter (d_{jet})	0.1δ	
Pitch angle (α)	$45°$	
Skew angle (β)	$-90°$	
Jet-jet spacing (D)	$8d_{\mathrm{jet}}$	
APR ($P_{\mathrm{oj}}^{\mathrm{pl}}/P_o$)	1	

B. Flow measurement techniques

In our study, we use both traditional surface-flow visualizations and more advanced nonintrusive optical measurement techniques. The surface flow topology was primarily evaluated using an oil-flow visualization technique, for which a mixture of hydraulic oil, oelic acid, and TiO_2 particles was applied to the wind-tunnel model prior to each run. A PCO Pixelfly camera mounted above the top-wall optical access acquired the transient oil-flow pattern, from which we extracted images with a resolution of 0.20 px/mm for processing and analysis.

Additionally, quantitative flow diagnostics were carried out using our 2C-2D-particle image velocimetry (PIV) system. We used a Litron NANO-L pulsed double-cavity Nd:YAG laser to illuminate a $12\delta \times 6\delta$ measurement plane as depicted in Fig. 2(a). The images were acquired using four Dantec FlowSense EO 11M cameras, each equipped with a Tamron SP AF 180m $f/3.5$ objective. The effective image acquisition rate was 6 Hz, and the laser pulse separation was set to 1 μs. To seed the flow, di-ethyl-hexyl-sebacate (DEHS) particles were generated, filtered, and introduced into the reservoir balloon prior to each run, using an in-house particle generator and a cyclone separator. Further details on the PIV setup and acquisition parameters are available in Ref. [20] (see WN-PIV in the reference).

Measurements were carried out at two streamwise/wall-normal planes (WN1 and WN2), in the spanwise direction at $z = 0D$ and $z = -1.5D$, respectively. This corresponds to streamwise/wall-normal planes along the jet-orifice centreline (WN1) and between two jet-orifices (WN2), respectively. For each test case, ensembles of ∼700–1000 images were collected over a span of multiple days. We processed the obtained images with Dantec DynamicStudio 6.4, using an adaptive PIV algorithm. The final interrogation size was 32 px × 32 px with 75% overlap. Further details on PIV postprocessing can be obtained from Ramaswamy and Schreyer [20,34].

An estimate of measurement uncertainty is crucial to accurately interpret the measured data. We have carried out detailed uncertainty analyses of the measurement conditions, uncertainties due to PIV particle-response time, and an assessment of statistical uncertainties of the mean and turbulent fluctuating quantities in previous studies at similar flow and measurement conditions [17,20,34]. Furthermore, in addition to good agreement of the experimental data with the companion LES simulation in this study (see Sec. IV A), a detailed validation of the baseline 24° compression-ramp interaction was also carried out by a second independent LES under similar conditions [57], thereby providing further confidence in the measured dataset.

IV. RESULTS AND DISCUSSION

A. Incoming supersonic turbulent crossflow boundary layer

We compare profiles of the mean velocity and the root-mean-square (RMS) of the velocity fluctuations in the incoming zero-pressure-gradient turbulent boundary layer on the flat-plate surface obtained from the PIV measurements and the LES in Fig. 3. The mean velocity profiles are

(a) Mean velocity

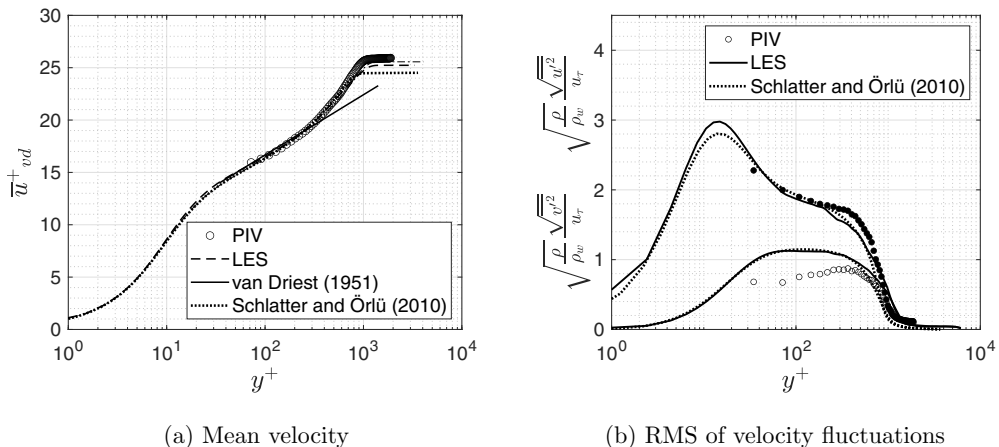(b) RMS of velocity fluctuations

FIG. 3. Incoming turbulent boundary-layer profiles.

transformed according to van-Driest [see Fig. 3(a)], and the Reynolds normal stresses are plotted in Morkovin scaling [see Fig. 3(b)] to allow for comparisons with reference direct-numerical-simulation (DNS) data of an incompressible turbulent boundary layer at $Re_\theta = 2540$ by Schlatter and Örlü [51]. The LES and PIV profiles, which have been independently validated against reference data from literature (see Refs. [34] and [12], respectively), are in good agreement with each other and with the reference DNS profiles. The resulting boundary-layer thicknesses and skin-friction coefficients are similar to within 9.5% and 6.9%, respectively. Table V summarizes the main boundary-layer parameters from both LES and PIV.

The PIV measurements slightly underpredict the wall-normal velocity fluctuations. Measurements of weak disturbances, such as the wall-normal velocity fluctuations, are particularly challenging with PIV [58]. However, such uncertainties are expected to diminish downstream of a shock wave, due to the associated increase in flow density and viscosity [59]; velocity profiles extracted downstream of the separation shock at the compression-corner interaction are therefore of higher accuracy.

B. Baseline 24° compression-ramp interaction

To better understand the effect of control discussed in Sec. IV E, we briefly introduce the baseline 24° shock-wave/boundary-layer interaction. The mean streamwise velocity contours and the RMS of streamwise velocity fluctuations of the baseline case are presented in Figs. 4(a) and 4(b), respectively. The origin of the streamwise coordinates are offset by $x_r = 7.69\delta$, which is equivalent to the distance between the jet-injection location and the ramp corner; the jets for the control cases

TABLE V. Flat-plate boundary-layer parameters.

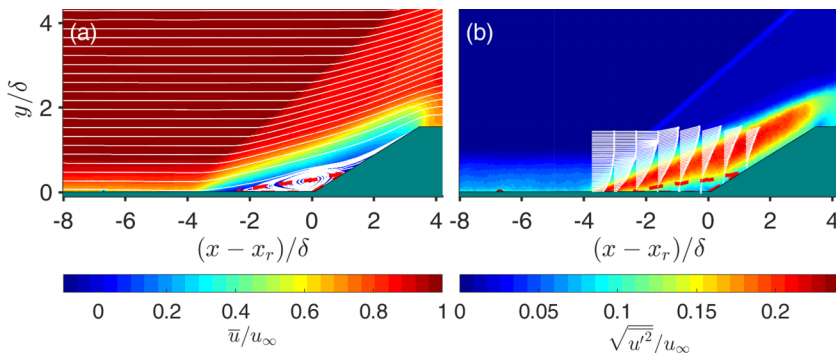| Parameter	LES [12]	PIV [34]
M_∞	2.5	2.52
Boundary-layer thickness (δ)	9.4 mm	10.4 mm
Re_θ	7000	8225
Re_τ	1093	1049
Friction velocity (u_τ)	25.32 m/s	25 m/s
Friction coefficient (c_f)	0.00186	0.00174

FIG. 4. (a) Normalized mean streamwise velocity and (b) normalized RMS of streamwise velocity fluctuations for the baseline case.

are thus injected at $x - x_r = -7.69\delta$. Boundary-layer profiles at selected locations are superimposed onto Fig. 4(b), and the red-dashed lines indicate the location of the zero-velocity streamline.

The incoming boundary layer experiences an adverse pressure gradient due to the separation shock and separates from the surface at $x - x_r \approx -2.5\delta$. The extrapolated location of the separation-shock foot is at $x - x_r \approx -4\delta$. The separated shear layer reattaches on the ramp surface at $x - x_r \approx 1.1\delta$, thereby enveloping a large region of reverse flow and a recirculation bubble (see red dashed lines). In addition to large mean-flow separation, the separated shear layer is also a source of pronounced turbulent fluctuations, as visualized in Fig. 4(b). For a detailed characterization of the baseline SWBLI, the reader is referred to Ramaswamy and Schreyer [20,34].

C. Flow in the jet-injection pipe

Prior to discussions on the jet-induced structures, we present a detailed characterization of the flow in the jet-injection pipe for the two cases in this section; such information is generally lacking in JISCF literature.

A large pressure difference exists between the plenum on one side and the crossflow on the other, which results in a rapid expansion of the flow in the jet pipe. The local Mach number is therefore a suitable parameter to discuss the characteristics of the pipe flow. Figures 5(a) and 5(b) depict the local Mach number contours for the SP and LP cases, respectively. The local axial and radial directions are represented using (ζ, ξ), with the jet exit into the crossflow at $\zeta = 0$ and the plenum/pipe interface at $\zeta = -4.24 d_{\text{jet}}$ and $\zeta = -18.38 d_{\text{jet}}$, respectively, for the two cases. Black lines in the figure represent the contour of $M_{\text{local}} = 1$. Due to the pressure difference between the plenum and the crossflow, the flow expands in the jet injection pipe. This expansion is more gradual for LP, due to longer pipe length. Close to the plenum/pipe intersection (P1), a local separation region forms with lower M_{local}.

The flow close to the jet exit on the flat-plate surface (P5) is supersonic with $M_{\text{local}} = 1.5$ for both cases. A plenum/pipe computational setup is thus able to provide more accurate jet-injection conditions than simply imposing or assuming a sonic jet-exit condition [28,29], as it is often done in JISCF literature.

Further details on the nature of jet injection can be obtained by studying the velocity evolution along the pipe. Mean axial velocity profiles from cases SP and LP, extracted at locations P1–P5, are shown in Fig. 5(c). Radial locations are denoted using ξ and are normalized with the jet diameter.

Close to the plenum/pipe intersection (location P1), the velocity is decreased for $\xi/d_{\text{jet}} \leqslant -0.3$ for both cases due to the local flow separation [see station P1 in Figs. 5(a) and 5(b)].

At $2d_{\text{jet}}$ downstream (location P2), the flow reattaches, however, the profiles are distinctly asymmetric: they exhibit two regions with higher velocities ($\xi/d_{\text{jet}} \sim 0.3$ and $\xi/d_{\text{jet}} \sim -0.4$) with
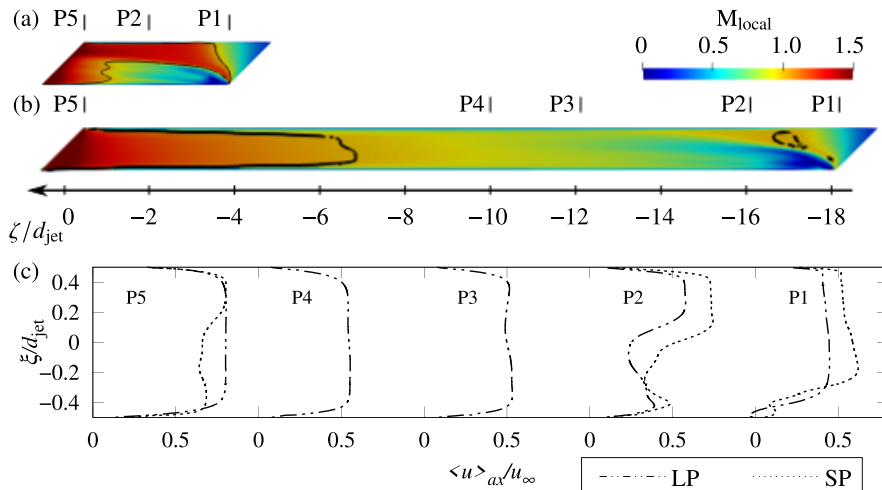
FIG. 5. Contours of the local Mach-number distribution superimposed with the isoline of $M_{local} = 1$ for case (a) SP and (b) LP in a spanwise/wall-normal plane at $x = 0$. (c) Evolution of mean axial velocity in the pipe at stations P1–P5.

a deficit close to the central region of the pipe. For the short pipe (case SP), the stronger flow expansion leads to an amplification of the velocity magnitude by approximately 30% at locations P1 and P2.

For the longer pipe LP, the asymmetry of the profile reduces significantly until location P3, and farther downstream, at location P4, the velocity profile indicates a developed pipe flow. These results indicate that the pipe should be at least $8d_{jet}$ long to allow for fully developed flow.

The differences in development length are still clearly visible at location P5 close to the jet exit on the flat-plate surface ($\zeta = 0$): while the profile for LP is symmetric and corresponding to a fully developed pipe flow, this is clearly not the case for SP. For case SP, the asymmetry is still significant, although it has decreased compared to location P2. The inflectional points in the velocity profile for this case indicate a possible instability due to the transitional flow in the pipe.

To better understand the characteristics of the flow in the jet-injection pipe, we extracted the relevant dynamic modes in the pipe flow by applying the DMD algorithm [53,54] to a temporal sequence of instantaneous flow fields. The DMD analysis was performed using 148 and 158 instantaneous snapshots equispaced in time with $\Delta \tilde{t} \tilde{u}_\infty / \tilde{d}_{jet} = 10$ for the SP and LP jet-flows, respectively, yielding a resolvable frequency range of $St = \tilde{f} \tilde{d}_{jet} / \tilde{u}_\infty = 0.00034$ to 0.05 for SP and $0.00032 \leqslant St \leqslant 0.05$ for LP. The DMD spectra of the injection-pipe flow for cases SP and LP are shown in Figs. 6(a) and 6(b), respectively. The real part (λ_r) of the spectrum represents the growth/decay rate, while the imaginary part (λ_i) indicates the the angular frequency. For both cases, we selected two representative modes [blue squares in Figs. 6(a) and 6(b)] from the subset that was detected using the sparsity-promoting algorithm of Jovanović et al. [55] [plus markers in Figs. 6(a) and 6(b)].

The eigenvalues and corresponding characteristic frequencies of the respective two selected modes for both cases are presented in Table VI.

For the SP case, mode Φ_1 is stable with $\lambda_r = -0.00032$, whereas Φ_2 is unstable with $\lambda_r = 0.00006 > 0$. Figures 6(c) and 6(d) show the spatial representation of pressure-fluctuation fields for both modes in a spanwise/wall-normal plane at $x = 0$. These modes have similar spatial representation with stronger pressure fluctuations in the region close to the sonic line [see also Fig. 5(a)]. The presence of an unstable DMD mode, in addition to the occurrence of inflection
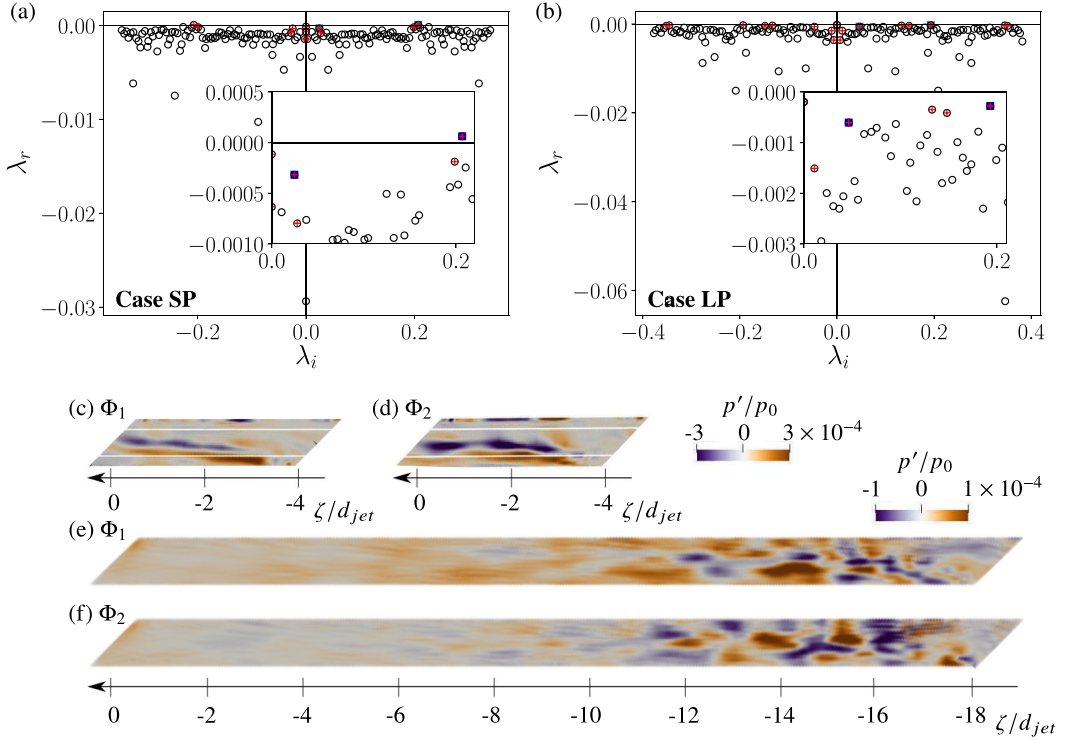
FIG. 6. [(a) and (b)] DMD spectra of the flow in the jet-injection pipe (○: DMD modes; +: sparsity-promoted DMD modes; ■: selected modes). Pressure fluctuation field of mode (c) Φ_1 and (d) Φ_2 for case SP and [(e) and (f)] for case LP.

points in the velocity profile close to the jet-exit plane [see Fig. 5(c)], is likely an indication of inflectional instability of the flow in the pipe.

Unlike for case SP, all modes of case LP are stable with $\lambda_r < 0$. Spatial representations of the two selected modes are similar [see Figs. 6(e) and 6(f)], with pressure fluctuations mainly in the region close to the pipe entrance; this is related to the energetic turbulent eddies which disintegrate in the downstream evolution. The overall fluctuation level for case LP is only 30% of that of case SP.

D. Single spanwise-inclined jet in a supersonic crossflow

Statistical and dynamical analyses of the jet-pipe flow in the previous section revealed vastly different flow topologies and dynamics for the two jet-pipe lengths, in-spite of similar plenum and crossflow conditions. In this section, we explore the effects of the jets on the crossflow in detail to

TABLE VI. Selected dynamically dominant modes for the two pipe flows.

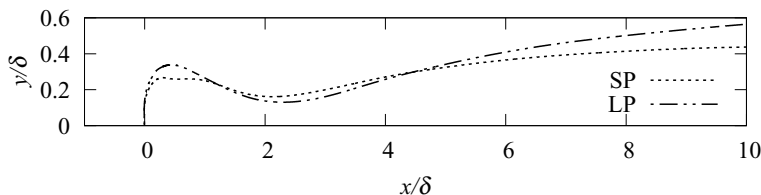| Case	Modes	λ	St
SP	Φ_1	$-0.00032 + 0.02456i$	0.0037
	Φ_2	$+0.00006 + 0.20667i$	0.0258
LP	Φ_1	$-0.00060 + 0.04642i$	0.0058
	Φ_2	$-0.00028 + 0.19314i$	0.0241

FIG. 7. Comparison of jet penetration into the crossflow.

(a) identify any changes in JISCF topology and characteristics and (b) study the impact of jet-pipe length on the jet-induced structures.

1. General flow topology

The jet-penetration depth into the crossflow has wide implications in flow-control applications. Figure 7 compares the jet-penetration depths into the crossflow for the two cases. The jet penetration was estimated on the basis of the trajectory of the streamline passing through the jet center, at the exit on the flat-plate surface. In close vicinity of the injection location ($x < \delta$), the penetration depth is slightly larger for the LP case. In the near field of the injection ($1 \leqslant x/\delta \leqslant 5$), a similar penetration depth is observed for both cases. In the far field, the penetration depth keeps increasing very slowly, until it seems to stagnate for $\delta \geqslant 9$ for the SP case, whereas for case LP, the penetration depth keeps increasing until $y = 0.6\delta$ at $x = 10\delta$, and is approximately 40% larger than for SP jet injection. In contrast to the conditions in other established JISCF literature [23], both jets remain within the boundary layer when adopted in an AJVG configuration, which is beneficial for flow-control purposes; the jets are expected to induce minimal parasitic drag, particularly in comparison with traditional mechanical vortex generators [4].

When injected into the crossflow, the jet interacts with the incoming supersonic boundary layer, which results in the formation of a complex system of shocks, separation zones, and an ensemble of vortical structures downstream. The shock structures can be identified by visualizing the mean density gradient in a spanwise/wall-normal plane at $x = 0$. Figures 8(a) and 8(b) show such
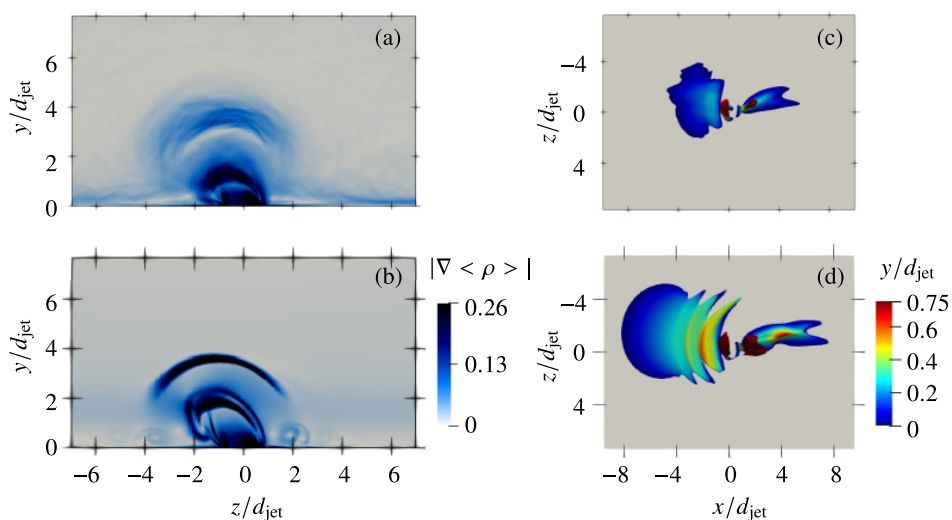

FIG. 8. [(a) and (b)] Mean density-gradient in the y-z plane at $x = 0$ and [(c) and (d)] isosurface of $\bar{u} = 0$ colored with y/d for [(a) and (c)] case SP and [(b) and (d)] case LP.

distributions for the SP and LP cases, respectively. Apart from small differences in the near field, the overall topologies are similar for both cases; and they are also fairly similar to that of wall-normal jets, albeit distinctly asymmetrical (see also Sebastian *et al.* [12]).

Due to the blockage of the incoming supersonic crossflow by the jet, a bow shock wave forms ahead of the jet on jet injection. The jet expansion is supported by a barrel shock that terminates in a Mach disk, an envelop shock forms downstream as a result of flow reattachment (not visible in Fig. 8; see Sebastian *et al.* [12] for details). The angles of the bow and the envelop shocks with respect to the x axis are approximately $30°$ and $25°$, respectively, for both cases (not shown here). However, the bow shock (see Fig. 8), as well as the barrel shock and the Mach disk are stronger and defined more clearly for case LP than for SP. The jet-exit pressure and density are approximately 15% lower for the long-pipe case; as a result, the mean velocity increases by 7%, so that the flow rate is maintained (see Table II). This prompts a higher degree of expansion at the jet exit and thus helps explain the stronger barrel shock and Mach disk. Such a stronger barrel-shock and Mach disk can result in enhanced vortex generation as a result of jet/crossflow interactions [30].

The obstruction imposed by the jet onto the incoming crossflow also results in a small separation zone around the jet orifice. The separation regions for the SP and LP cases are visualized using the isosurface of $<u> = 0$ in Figs. 8(c) and 8(d), respectively. The 3D separation regions for case LP are larger and taller than for case SP. These effects could be related to the enhanced local jet penetration at $x = 0$. The upstream and downstream separation regions for case LP extend up to $y = 0.55d_{jet}$ and $0.7d_{jet}$, respectively, whereas, for SP, they are limited to within $y = 0.15d_{jet}$ and $0.3d_{jet}$. Similarly, the streamwise extents of both separation regions are approximately 60% larger for case LP, and the spanwise extent of the upstream bubble is 16% larger compared to that of case SP. The spanwise width of the quasi-herringbone-shaped downstream separation bubble is almost identical for both cases, however, for the LP case, it is streamlined with the crossflow.

Moreover, the topology of the upstream separation region is more complex, with saw-tooth like features at the lateral edges.

2. Jet-induced coherent vortical structures

On jet injection, an ensemble of vortices is induced in the boundary layer. The strength and longevity of these vortices directly influence the momentum exchange within the boundary layer, and therefore the flow-control effectiveness, when adopted in an AJVG configuration. The vortical structures for both the SP and LP cases are visualized by means of the isosurface of the Q criterion for $Q = 0.07$ in Fig. 9. The major CVP is the most prominent vortical structure; others include a secondary counter-clockwise rotating upper-trailing vortex, a surface-trailing CVP, and primary and secondary horseshoe vortices [12]. Except for the major CVP, the other jet-induced vortices either merge or dissipate quickly and are thus of little consequence in the context of flow control. Therefore, irrespective of the vortex-generation mechanism, the major CVP is primarily responsible for the desired increase in momentum exchange and thus directly contributes to enhancing the boundary layer's ability to resist separation [12].

The vortical structures for the LP case [see Fig. 9(b)] are more coherent and have longer lifespan than for the short-pipe case [see Fig. 9(a)]. The major CVP, in particular, has a $\sim$30% longer lifespan for the LP case. Furthermore, the LP case exhibits also much more elongated and complex horseshoe vortices, which extend up to $x = 20d_{jet}$. A primary and two secondary horseshoe vortices are observed; these appear to be responsible for the saw-tooth pattern of the upstream separation region shown in Fig. 8(d).

For a more quantitative comparison of the CVPs, we compare the spanwise/wall-normal distribution of the mean streamwise vorticity for the two cases at $x = 0.5\delta$ and 2δ in Fig. 10. Vectors of $<v> - <w>$ are superimposed onto the vorticity contours to help identify the major vortical structures.

The jets are injected in the $-z$ direction. Due to this spanwise-inclined injection, the major CVP is asymmetric and the clockwise-rotating major vortex lies over the counter-clockwise rotating vortex.
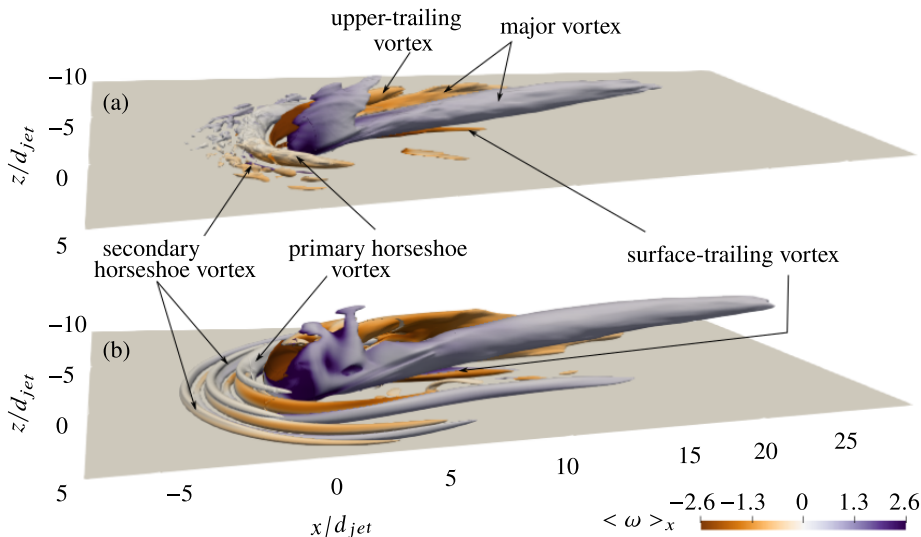
FIG. 9. Isosurface of Q criterion ($Q = 0.07$) colored with mean streamwise vorticity magnitude($< \omega >_x$) for (a) case SP and (b) case LP.

The longer-pipe case [see Figs. 10(b) and 10(d)], with a fully developed flow in the injection pipe, generates a stronger and more pronounced CVP than the short-pipe case [Fig. 10(a) and 10(c)].

This stronger CVP for the LP case is linked to an enhanced generation of instantaneous hairpinlike vortices. Previous JISCF studies have identified regions of vortex formation in the shear layer on the windward and leeward sides of the jet, where hairpinlike structures are generated [30]. The roll-up of these vortices has been linked to the formation of CVPs in the time-averaged sense [60]: These instantaneous hairpin vortices dominate in the vicinity of the jet, as well as in the process where these shear-layer vortices begin to roll-up, thereby engulfing the crossflow, and then subsequently mix with the crossflow. This combined effect leads to the formation of major CVP, and the process continues even after the formation of the major CVP [30].

Moreover, such instantaneous formation of vortices is often coupled with the incoming boundary layer and the dynamics of the shock structure [30]. With the stronger and potentially more dynamic barrel shock and Mach disk for the LP case [see Figs. 8(a) and 8(b) and associated discussions], the resulting flow can enhance the generation of these instantaneous hairpinlike vortices and thereby cause the observed formation of stronger CVPs.
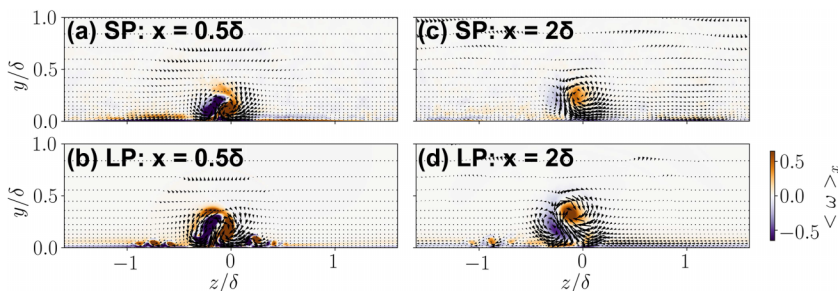

FIG. 10. Spanwise/wall-normal distribution of mean streamwise vorticity at [(a) and (b)] $x = 0.5\delta$ and [(c) and (d)] $x = 2\delta$ for cases [(a) and (c)] SP and [(b) and (d)] LP, respectively.
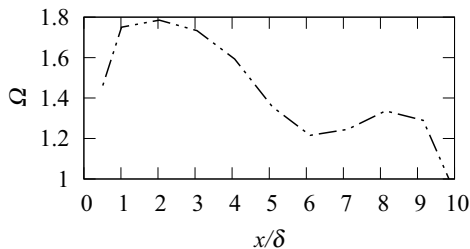
FIG. 11. Evolution of maximum vorticity ratio $\Omega = \max(<\omega>_x^{\mathrm{LP}})/\max(<\omega>_x^{\mathrm{SP}})$.

In the context of flow control, a stronger vorticity of the streamwise vortices can improve the flow-control effectiveness. For a direct comparison of the two cases, and to quantify the evolution of vorticity in the streamwise direction, we plot the streamwise evolution of the ratio of maximum streamwise vorticity in the LP and SP cases ($\max(<\omega>_x^{\mathrm{LP}})$ and $\max(<\omega>_x^{\mathrm{SP}})$, respectively) in Fig. 11. For this, the clockwise-rotating major vortex was isolated due to its prominence in spanwise-inclined injection setups [12]. In the near-field region ($x \leqslant 3.5\delta$), case LP has a 75% stronger vorticity than case SP. Farther downstream ($3 \leqslant x/\delta \leqslant 6$), the vorticity ratio ($\Omega$) drops considerably from $\Omega = 1.8$ to $\Omega = 1.2$. Beyond $x > 6\delta$, Ω is small with less than 20% improvement in vorticity over the SP case.

E. Separation control using an array of jets

In the previous sections, we assessed LESs of two spanwise-inclined single-JISCF cases with different injection-pipe lengths to identify differences in flow structure and topology. We found that (a) injection-pipe lengths of at least $8d_{\mathrm{jet}}$ result in fuller jet-velocity profiles without inflection points, (b) jets injected from such pipes into the crossflow lead to stronger bow and barrel shocks and a well-defined Mach disk, (c) the resulting jet-induced structures are coherent for a longer downstream distance, and (d) the major CVPs for these cases with a fully developed jet (LP) are up to 75% stronger than for jets from shorter injection pipes (SP) with underdeveloped flow. We therefore expect an increase in momentum exchange and consequently better flow-control effectiveness, when LP jets are used as AJVGs. Most AJVG setups employ a spanwise series of jets, i.e., an array configuration (see, e.g., Refs. [14,15,21,34,56]). For such configurations, the inter-jet spacing (D) and the injection pressure ($P_{\mathrm{oj}}^{\mathrm{pl}}$) play a prominent role in defining the degree of interaction between neighboring jets [19], and thereby govern the control effectiveness in addition to the traditional JISCF parameters associated with single jets. The control effectiveness is most favorable for spacings of $D \approx 7d_{\mathrm{jet}} - 13d_{\mathrm{jet}}$ and injection pressures of $P_{\mathrm{oj}}^{\mathrm{pl}} \approx 0.85P_o - 1.75P_o$ [20,22,48]. Such interacting jets amplify the jet-induced vorticity, and the associated structures increase local down-wash, which leads to delayed vortex lift-off [48].

Since the jet-induced vortices are stronger for the LP than the SP case, we expect the LP jets to further enhance the streamwise vorticity when employed in an array configuration with optimal jet/jet interaction; LP jets should therefore be favorable for separation-control applications. To test this hypothesis, we applied two jet-array setups with different jet injection-pipe lengths and otherwise identical parameters to control a $24°$ compression-ramp-induced separation; we analyzed these configurations experimentally (see Sec. III) under the same geometrical and flow conditions as the single-jet LESs (see Sec. II).

Note that the larger diameter of the CVP in case LP (see Fig. 10) may also play a role in the interplay between the jet spacing and injection pressure that determines the jet/jet interaction strength and thus the AJVG control effectiveness (see Sebastian et al. [22]). The major CVP is larger and stronger in the LP than in the SP case (see Figs. 10 and 11), which could amplify the jet/jet interactions in an array configuration [22,48]. The diameter of the major CVP at $x = 0.5\delta$ in the LP
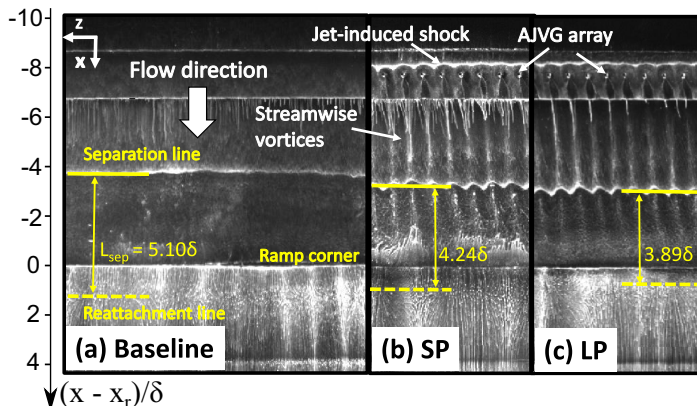
FIG. 12. Separation-control effectiveness of the AJVG arrays.

case is $6.5d_{\text{jet}} \approx 0.65\delta$; this diameter is 8% larger than in the present SP case [see Figs. 10(a) and 10(c)] and equivalent to our previously studied short-pipe case with $P_{\text{oj}}^{\text{pl}} = 1.5P_0 (\equiv 25.5P_\infty)$ under otherwise consistent conditions (see Ref. [22]). For the latter case, optimal control effectiveness was achieved for jet spacings between $8d_{\text{jet}} \leqslant D \leqslant 10d_{\text{jet}}$ [22]. Moreover, the vorticity is stronger in the present LP case than in our earlier short-pipe case with $P_{\text{oj}}^{\text{pl}} = 1.5P_0$. These combined effects would allow for slightly larger jet spacings for LP jets without compromising their control effectiveness. A larger spacing would thus also make the setup more energy efficient and sustainable.

However, we use a consistent jet spacing of $D = 8d_{\text{jet}}$ for both injection-pipe cases in the following experimental study, since we do not have enough data to separate the effects of CVP size and strength on the control effectiveness, as well as to allow for direct comparisons with literature data and our earlier AJVG-control studies.

1. Flow topology and effect of jet-exit flow on the separation-control effectiveness

To obtain a first overview on the flow topology and the flow-control effectiveness of the two jet arrays, we used oil-flow visualizations to identify the major surface features. Figure 12 shows the surface-flow topology of the SP and LP AJVG cases. The uncontrolled baseline compression-ramp interaction is also shown for comparison. For the baseline interaction, the nearly 2D line of oil accumulation upstream of the ramp corner helps to identify the flow-separation line (solid yellow line), while a spanwise series of saddle points on the ramp surface indicates the flow-reattachment line (dashed yellow line). The total length of separation measured along the ramp surface was 5.1δ.

For the AJVG-control cases, a distinct jet-induced bow shock-wave and local separation region form upstream of each jet. Unlike for the single jet cases discussed in Sec. IV D 1, the separation regions induced by each jet in the array merge in the spanwise direction and form one larger spanwise corrugated separation zone upstream of the jet orifices. For the two studied control cases, the mean flow separation upstream of the jet orifices does not measurably differ; this result was expected, since any changes will be less than $O(d_{\text{jet}})$ and therefore challenging to perceive from oil-flow visualizations.

Downstream of jet injection, a spanwise series of streamwise vortices forms, which are visible as stagnant lines of oil in Figs. 12(b) and 12(c). The streamwise vortices modulate the boundary layer and enhance mixing. Consequently, the originally 2D separation line is now corrugated. While the general topology remains similar for both cases, the locations of flow-separation and reattachment lines for the two cases clearly and measurably differ. We extracted the separation and reattachment locations along one jet pitch (i.e., one inter-jet spacing) from the model center-line $(-0.5D \leqslant z = 0 \leqslant 0.5D)$ from multiple frames of the oil-flow visualization to calculate the

TABLE VII. Total separation length (L_{sep}) for all cases.

| Case	L_{sep}	$(L_{\text{sep}:b} - L_{\text{sep}:c})/L_{\text{sep}:b}$	σ/δ
Baseline	$5.10\delta \pm 1.51\%$	—	—
SP	$4.24\delta \pm 1.82\%$	17%	0.23
LP	$3.89\delta \pm 1.97\%$	24%	0.29

corresponding mean locations (see Table VII). The difference (σ) between the maximum and minimum separation lengths along one jet pitch was also extracted to represent the degree of corrugation of the separation line. This technique prevents misinterpretations due to edge effects at either end of the AJVG array. Furthermore, the mean resulting from this technique is equivalent to the spanwise-averaged separation length over the central 30% of the AJVG array [17].

While the SP case achieves a reduction in mean separation length of approximately 17%, the LP case with its fuller jet-velocity profile and stronger jet-induced streamwise vorticity achieves a reduction of approximately 24%. The corrugation of the separation line is very similar for both cases.

2. Mean-flow modification downstream of jet injection

To better interpret the trends observed in the oil-flow visualizations, we conducted PIV measurements in the streamwise/wall-normal plane at two spanwise locations – WN1 located along the jet centerline at $z = 0D$ and WN2 located in-between two jet-orifices at $z = -1.5D$. The resulting mean boundary-layer profiles for the two jet-injection-pipe-length cases at selected streamwise locations across the SWBLI are shown in Fig. 13. Profiles are shown at locations (a) downstream of jet injection but upstream of the separation-shock foot: $x - x_r = -6\delta, -4.5\delta$; (b) within the separated shear layer: $x - x_r = -3\delta$; and (c) downstream of flow reattachment on the ramp surface: 3δ. Note that the velocities along the ramp surfaces are resolved and presented along the ramp-surface parallel and ramp-normal coordinate axes (x^*, y^*).

Downstream of jet injection, at $x - x_r = -6\delta$ [see Figs. 13(a) and 13(e)] and $x - x_r = -4.5\delta$ [see Figs. 13(b) and 13(f)], the flow-entrainment effect of the streamwise vortices is visible in the
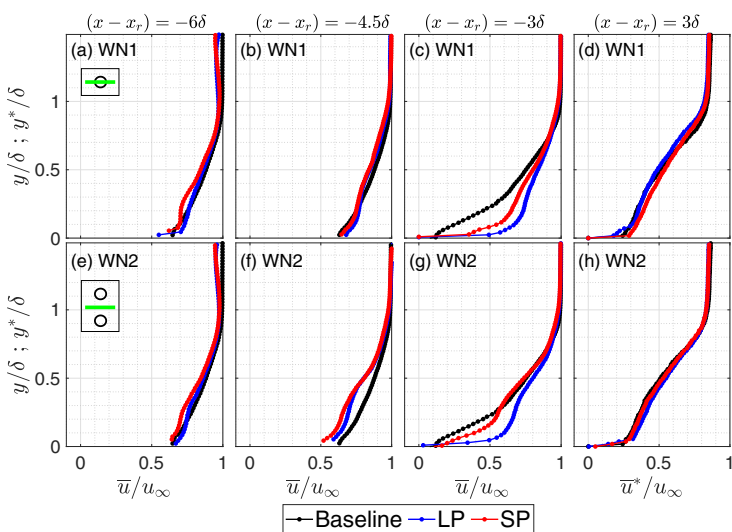
FIG. 13. Normalized mean streamwise velocity distributions. Ramp corner: $x_r = 7.69\delta$.
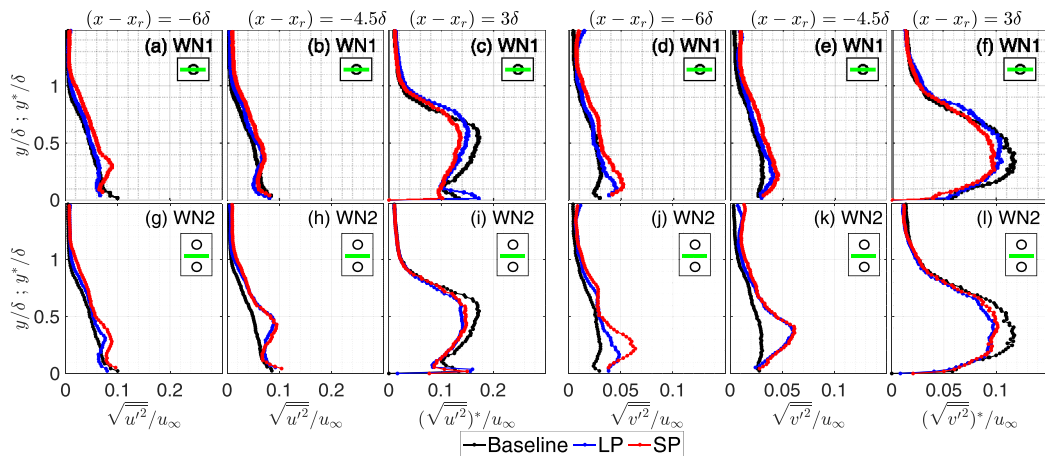
FIG. 14. Normalized RMS of streamwise [(a)–(c) and (g)–(i)] and wall-normal [(d)–(f) and (j)–(l)] velocity fluctuations at three streamwise locations. WN1 [(a)–(f)]; WN2 [(g)–(l)]; Ramp corner: $x_r = 7.69\delta$.

distinctly S-shaped mean velocity profiles at both WNI and WN2. At both these locations, the velocities close to the wall clearly are larger for case LP than for jet-injection case SP. The LES results (see Sec. IV D) show the formation of stronger and more coherent jet-induced structures for the LP case. Furthermore, simulations of Sebastian and Schreyer [48] have highlighted that favorable jet/jet interactions amplify the jet-induced vorticity and further improve entrainment. A combination of these effects explain the higher velocities close to the wall for the LP jet-array case in this study.

These differences in the degree of entrainment between cases LP and SP lead to a disparity in separation-shock-induced flow deceleration at $x - x_r = -3\delta$ [see Figs. 13(c) and 13(g)]. The baseline case experiences the largest velocity declaration due to an earlier ramp-induced separation. For cases SP and LP, however, the separation-line moves downstream (see Fig. 12) and therefore they experience lower velocity deceleration than the baseline case. As the onset of separation is farther downstream for case LP than for case SP, the velocity profiles at $x - x_r = -3\delta$ are fuller for case LP than for the baseline and SP cases. These findings support the observations made from the oil-flow visualizations by showing a clear difference in the onset of flow separation.

Downstream of the interaction with the ramp-induced shock, the flow reorganizes, and Görtler-like vortices are formed (see Refs. [46,61–63]). In the interaction region, the momentum redistribution by the Görtler-like vortices is enhanced by additional momentum introduced by the jets. This effect leads to flow homogenization (in the spanwise direction) downstream of the separation shock and earlier flow reattachment in AJVG control with jets from short pipes [46]. We made similar observations for case LP [see the velocity profiles at the ramp corner shown in Figs. 13(d) and 13(h)], where no major differences in the velocity profiles between WN1 and WN2 are visible. Jet injection has negligible influence on the recovering boundary layer after the interaction with the separation shock [46]. Therefore, the effects of jet-pipe length and jet-exit velocity profile diminish in the downstream evolution and the boundary layer begins its recovery back to the equilibrium state (not shown here).

3. Turbulence statistics

Differences in the jet-injection velocity profiles not only affect the mean-flow topology, but also the turbulence structure and behavior downstream of jet injection. The streamwise evolution of the RMS of the streamwise and wall-normal velocity fluctuations at selected streamwise locations across the SWBLI is presented in Fig. 14.

At about 1.7δ downstream of the jet-injection location ($x - x_r = -6\delta$), the SP jet-injection case shows a peak in $\sqrt{u'^2}$ at $y = 0.3\delta$ at the WN1 location [see Fig. 14(a)], which is $\sim$50% stronger than the peak $\sqrt{u'^2}$ of the LP case at the same location. This increase in turbulence intensity is most likely related to small-scale turbulence that is generated when the underdeveloped jet-velocity profile at the pipe exit in case SP is injected into the crossflow; this small-scale turbulence is absent for jet injection with a fully developed jet. Stronger RMS intensities at this streamwise location for the SP case also occur for $\sqrt{u'^2}$ at WN2 [see Fig. 14(g)] and for $\sqrt{v'^2}$ at WN1 [see Fig. 14(d)] and WN2 [see Fig. 14(j)].

With downstream flow evolution ($x - x_r = -4.5$), the small-scale turbulence dissipates, and the SP and LP cases collapse [see Figs. 14(b) and 14(h) and Figs. 14(e) and 14(k)]. However, the mean-velocity profiles at this location are fuller for the LP than for the SP jet-injection cases [see Figs. 13(b) and 13(f)]. The favorable effect of the LP case on the separation-control effectiveness thus is primarily brought about by the stronger jet-induced vorticity, which is augmented by the favorable interactions between the jets in the array. The turbulent mixing brought about by the small-scale turbulence generated in the short-pipe case on the boundary layer momentum-exchange is likely a weaker influence here.

At all other downstream locations (not shown), the effects of SP and LP jet injection on the boundary layer turbulence are similar and follow the trends of the baseline case [similar to the profiles at $x - x_r = 3\delta$ in Figs. 14(c) and 14(i) and Figs. 14(f) and 14(l)].

V. CONCLUDING REMARKS

We assessed modifications in the jet-in-supersonic-crossflow characteristics brought about by changes in the jet-exit flow that were caused by modified jet-injection-pipe lengths. Also the associated influences on separation-control effectiveness when such jets were used as air-jet vortex generators were analyzed. A combined experimental-computational approach has been chosen. First, we carried out LESs of two single spanwise-inclined JISCF configurations with different jet-pipe lengths but otherwise equivalent plenum and crossflow conditions. A fully turbulent flat-plate boundary layer at Mach 2.5 and $\mathrm{Re}_\theta = 7000$ served as the crossflow. The jets were injected from a circular orifice of diameter $d_{\mathrm{jet}} = 0.1\delta$, which was inclined at $45°$ in the spanwise/wall-normal direction. The plenum pressure was equal to the crossflow total pressure.

The topology of the flow in the injection pipe is vastly different for the different pipe lengths. For the short pipe with a length of $l = 4.24d_{\mathrm{jet}}$ (case SP), the jet flow is underdeveloped, and the axial velocity profile of the jet at the exit plane features inflection points. Furthermore, the presence of unstable modes was revealed by a DMD analysis carried out on a sequence of the pipe flow. In contrast, the flow expansion was more gradual for the longer-pipe case ($l = 18.38d_{\mathrm{jet}}$; case LP). The flow at the jet exit is fully developed and no unstable modes were detected by DMD. For both cases, the exit Mach number was supersonic. For the current conditions, a pipe length of at least $8d_{\mathrm{jet}}$ is necessary to achieve a fully developed and stable flow in the pipe.

Both jet cases induce qualitatively similar shocks, separation zones, and vortical structures. The strength and coherence of the jet-induced flow topology, however, varies with pipe length and exit velocity profile. The bow shock, barrel shock, and Mach disk are stronger for case LP, and the jet-induced separation is nearly 60% longer. On the basis of isosurfaces of the Q criterion, we detected vortical structures with a longer lifespan for case LP. Furthermore, the longer-pipe case (LP) with fully developed jet flow generates a more well-defined and stronger major CVP than case SP with underdeveloped pipe flow. Consequently, the streamwise vorticity is increased by up to 75% for case LP in comparison to case SP.

Therefore, we assumed that the longer jet-pipe case, with its fully developed jet velocity profile and favorable JISCF characteristics, can improve the flow-control effectiveness when used in an AJVG-control configuration. To test this hypothesis, we installed a spanwise series of LP jet-orifices in an AJVG setup to control a $24°$ compression-ramp-induced SWBLI and studied it experimentally.

The experiments were carried out at plenum and crossflow conditions equivalent to those of the LES. The spanwise-inclined jets were spaced $8d_{jet}$ apart in the spanwise direction; this arrangement has been identified as favorable in previous studies [19,48]. The jet total pressure was equal to the wind-tunnel total pressure. For comparison, also a SP setup was investigated—the two cases were equivalent to the cases studied with LES (case SP with a pipe length of $l = 4.24d_{jet}$, case LP with $l = 18.38d_{jet}$).

Oil-flow visualizations of the two test cases show a corrugation of the ramp-induced separation line due to the jet-induced streamwise vortices. While the short-pipe case achieves a 17% reduction in total separation length, the longer jet-injection pipe achieves nearly 24% of reduction (both in comparison with the baseline case). The boundary-layer development downstream of the jet-injection and across the SWBLI was assessed on the basis of PIV measurements in streamwise/wall-normal planes at two spanwise locations. The mean-velocity profiles downstream of the jet injection and upstream of the ramp-induced separation shock show higher velocities close to the wall and evidence of increased entrainment for the LP case. This behavior is likely a result of the stronger and more coherent jet-induced vortices in the LP case, and it is further augmented with even more favorable jet/jet interactions for this case.

The RMS values of the velocity fluctuations are higher for the short pipe, most probably due to small-scale turbulence; these high fluctuations quickly dissipate downstream and do not contribute to any increase in turbulent mixing within the boundary layer. At the ramp corner and at locations along the ramp surface, effects caused by the jet-velocity profile diminish, and the mean and turbulent velocity profiles collapse for both tested cases.

The present study shows direct consequences of the strength and downstream longevity of streamwise vortices induced by a flow control device on its separation-control effectiveness. While this effect was demonstrated on the basis of air-jet vortex generators, it should in principle also be applicable to other vortex-generator devices. An improved performance can be expected from vortex generators that are optimized to enhance the vorticity magnitude at minimal impact to the external flow. The present results also indicate the strong influence of the state and development of the flow in the jet-injection pipe on the jet-in-supersonic-crossflow field. Therefore, this part of the geometry and setup needs to be carefully taken into account and documented in any study and application using jet-in-supersonic-crossflow configurations, e.g., for turbulent mixing or fuel-injection purposes.

ACKNOWLEDGMENTS

[1] D. S. Dolling, Fifty years of shock-wave/boundary-layer interaction research: What next? AIAA J. **39**, 1517 (2001).

[2] N. T. Clemens and V. Narayanaswamy, Low-frequency unsteadiness of shock wave/turbulent boundary layer interactions, Annu. Rev. Fluid Mech. **46**, 469 (2014).

[3] J. M. Delery, Shock wave/turbulent boundary layer interaction and its control, Prog. Aerosp. Sci. **22**, 209 (1985).

[4] H. Pearcey, Introduction to shock-induced separation and its prevention by design and boundary layer control, in *Boundary Layer and Flow Control*, edited by G. Lachmann (Pergamon, Oxford, 1961), pp. 1166–1344.

[5] J. C. Lin, Review of research on low-profile vortex generators to control boundary-layer separation, Prog. Aerosp. Sci. **38**, 389 (2002).

[6] P. Dupont, C. Haddad, J. Ardissone, and J. Debiève, Space and time organisation of a shock wave/turbulent boundary layer interaction, Aerosp. Sci. Technol. **9**, 561 (2005).

[7] M. J. Lighthill and M. H. A. Newman, On boundary layers and upstream influence. i. a comparison between subsonic and supersonic flows, Proc. R. Soc. Lond. A **217**, 344 (1953).

[8] G. J. Harloff and G. E. Smith, Supersonic-inlet boundary-layer bleed flow, AIAA J. **34**, 778 (1996).

[9] H. Taylor, The elimination of diffuser separation by vortex generators, Technical Report No. R-4012-3 (United Aircraft Corporation, 1947).

[10] R. A. Wallis, The use of air jets for boundary layer control, Tech. Rep. (Aerodynamic Research Lab, Aerodynamic Notes 110, Australia, 1952).

[11] Y. Kamotani and I. Greber, Experiments on a turbulent jet in a cross flow, AIAA J. **10**, 1425 (1972).

[12] R. Sebastian, T. Lürkens, and A.-M. Schreyer, Flow field around a spanwise-inclined jet in supersonic crossflow, Aerosp. Sci. Technol. **106**, 106209 (2020).

[13] J. P. Johnston and M. Nishi, Vortex generator jets—Means for flow separation control, AIAA J. **28**, 989 (1990).

[14] R. Szwaba, Comparison of the influence of different air-jet vortex generators on the separation region, Aerosp. Sci. Technol. **15**, 45 (2011).

[15] R. Szwaba, Influence of air-jet vortex generator diameter on separation region, J. Therm. Sci. **22**, 294 (2013).

[16] R. Sebastian and A.-M. Schreyer, Flow fields around spanwise-inclined elliptical jets in supersonic crossflow, Eur. J. Mech. B Fluids **94**, 299 (2022).

[17] D. P. Ramaswamy and A.-M. Schreyer, Separation control with elliptical air-jet vortex generators, Exp. Fluids **64**, 105 (2023).

[18] D. P. Ramaswamy and A.-M. Schreyer, Effects of jet-orifice shape on the flow-control effectiveness of air-jet vortex generators, in *Notes on Numerical Fluid Mechanics and Multidisciplinary Design* (Springer, Cham, 2023), pp. 99–108.

[19] D. P. Ramaswamy, R. Hinke, and A.-M. Schreyer, Influence of jet spacing and injection pressure on separation control with air-jet vortex generators, in *Notes on Numerical Fluid Mechanics and Multidisciplinary Design* (Springer, Berlin, 2019), pp. 234–243.

[20] D. P. Ramaswamy and A.-M. Schreyer, Effects of jet-to-jet spacing of air-jet vortex generators in shock-induced flow-separation control, Flow, Turbul. Combust. **109**, 35 (2022).

[21] S. B. Verma and C. Manisankar, Control of compression-ramp-induced interaction with steady microjets, AIAA J. **57**, 2892 (2019).

[22] R. Sebastian, D. P. Ramaswamy, and A.-M. Schreyer, Spanwise-inclined jets in supersonic crossflow: Effects of injection pressure and separation-control effectiveness, AIAA J. **61**, 3833 (2023).

[23] K. Mahesh, The interaction of jets with crossflow, Annu. Rev. Fluid Mech. **45**, 379 (2013).

[24] M. R. Gruber, A. S. Nejad, T. H. Chen, and J. C. Dutton, Mixing and penetration studies of sonic jets in a mach 2 freestream, J. Propul. Power **11**, 315 (1995).

[25] J. G. Santiago and J. C. Dutton, Velocity measurements of a jet injected into a supersonic crossflow, J. Propul. Power **13**, 264 (1997).

[26] L. J. Souverein and J.-F. Debiève, Effect of air jet vortex generators on a shock wave boundary layer interaction, Exp. Fluids **49**, 1053 (2010).

[27] M. Y. Ali and F. Alvi, Jet arrays in supersonic crossflow—An experimental study, Phys. Fluids **27**, 126102 (2015).

[28] V. Viti, R. Neel, and J. A. Schetz, Detailed flow physics of the supersonic jet interaction flow field, Phys. Fluids **21**, 046101 (2009).

[29] M. B. Sun and Z. W. Hu, Generation of upper trailing counter-rotating vortices of a sonic jet in a supersonic crossflow, AIAA J. **56**, 1047 (2018).

[30] S. Kawai and S. K. Lele, Large-eddy simulation of jet mixing in supersonic crossflows, AIAA J. **48**, 2063 (2010).

[31] A. Ferrante, G. Matheou, and P. E. Dimotakis, LES of an inclined sonic jet into a turbulent crossflow at mach 3.6, J. Turbul. **12**, N2 (2011).

[32] X. Chai, P. S. Iyer, and K. Mahesh, Numerical study of high speed jets in crossflow, J. Fluid Mech. **785**, 152 (2015).

[33] Y. Liu, H. Zhang, and P. Liu, Flow control in supersonic flow field based on micro jets, Adv. Mech. Eng. **11**, 168781401882152 (2019).

[34] D. P. Ramaswamy and A.-M. Schreyer, Control of shock-induced separation of a turbulent boundary layer using air-jet vortex generators, AIAA J. **59**, 927 (2021).

[35] C. A. Hale, M. W. Plesniak, and S. Ramadhyani, Structural features and surface heat transfer associated with a row of short-hole jets in crossflow, Int. J. Heat Fluid Flow **21**, 542 (2000).

[36] S. D. Peterson and M. W. Plesniak, Evolution of jets emanating from short holes into crossflow, J. Fluid Mech. **503**, 57 (2004).

[37] T. H. New, T. T. Lim, and S. C. Luo, Effects of jet velocity profiles on a round jet in cross-flow, Exp. Fluids **40**, 859 (2006).

[38] S. Muppidi and K. Mahesh, Study of trajectories of jets in crossflow using direct numerical simulations, J. Fluid Mech. **530**, 81 (2005).

[39] A. Lintermann, M. Meinke, and W. Schroeder, Zonal flow solver (ZFS): A highly efficient multi-physics simulation framework, Int. J. Comput. Fluid Dyn. **34**, 458 (2020).

[40] M.-S. Liou and C. J. Steffen, A new flux splitting scheme, J. Comput. Phys. **107**, 23 (1993).

[41] M. Meinke, W. Schroeder, E. Krause, and T. Rister, A comparison of second- and sixth-order methods for large-eddy simulations, Comput. Fluids **31**, 695 (2002).

[42] V. Venkatakrishnan, Convergence to steady state solutions of the euler equations on unstructured grids with limiters, J. Comput. Phys. **118**, 120 (1995).

[43] J. P. Boris, F. F. Grinstein, E. S. Oran, and R. L. Kolbe, New insights into large eddy simulation, Fluid Dynam. Res. **10**, 199 (1992).

[44] W. El-Askary, W. Schroeder, and M. Meinke, LES of compressible wall-bounded flows, in *16th AIAA Computational Fluid Dynamics Conference* (American Institute of Aeronautics and Astronautics, Reston, VA, 2003).

[45] B. Roidl, M. Meinke, and W. Schröder, Numerical investigation of shock wave boundary-layer interaction using a zonal RANS-LES ansatz, in *High Performance Computing in Science and Engineering '10* (Springer, Berlin, Heidelberg, 2011), pp. 369–383.

[46] R. Sebastian and A.-M. Schreyer, Control of SWBLI in a 24deg compression ramp flow with air-jet vortex-generator, in *AIAA SCITECH 2023 Forum* (American Institute of Aeronautics and Astronautics, 2023).

[47] R. Sebastian and A.-M. Schreyer, Influence of crossflow mach number on spanwise-inclined jet injection, in *AIAA SCITECH 2022 Forum* (American Institute of Aeronautics and Astronautics, 2022).

[48] R. Sebastian and A.-M. Schreyer, Influence of jet spacing in spanwise-inclined jet injection in supersonic crossflow, J. Fluid Mech. **946**, A39 (2022).

[49] R. Sebastian and A.-M. Schreyer, Forced injection of a spanwise-inclined jet in supersonic crossflow, AIAA J. 1 (2023).

[50] R. Sebastian and A.-M. Schreyer, Forced control of SWBLI in a 24deg compression ramp flow with air-jet vortex-generator, in *AIAA AVIATION 2023 Forum* (American Institute of Aeronautics and Astronautics, 2023).

[51] P. Schlatter and R. Örlü, Assessment of direct numerical simulation data of turbulent boundary layers, J. Fluid Mech. **659**, 116 (2010).

[52] J. C. Hunt, A. A. Wray, and P. Moin, Eddies, streams, and convergence zones in turbulent flows, Studying turbulence using numerical simulation databases, 2, Proceedings of the 1988 summer program.

[53] C. W. Rowley, I. Mezić, S. Bagheri, P. Schlatter, and D. S. Henningson, Spectral analysis of nonlinear flows, J. Fluid Mech. **641**, 115 (2009).

[54] P. J. Schmid, Dynamic mode decomposition of numerical and experimental data, J. Fluid Mech. **656**, 5 (2010).

[55] M. R. Jovanović, P. J. Schmid, and J. W. Nichols, Sparsity-promoting dynamic mode decomposition, Phys. Fluids **26**, 024103 (2014).

[56] R. A. Wallis, On the control of shock-induced boundary-layer separation with discrete air jets, Technical Report No. CP 595 (Aeronautical Research Council, 1958).

[57] L. Larchevêque, D. P. Ramaswamy, and A.-M. Schreyer, Effects of favourable downstream pressure gradients on separated shock-wave/boundary-layer interactions, Int. J. Heat Fluid Flow **102**, 109164 (2023).

[58] O. J. H. Williams, T. Nguyen, A.-M. Schreyer, and A. J. Smits, Particle response analysis for particle image velocimetry in supersonic flows, Phys. Fluids **27**, 076101 (2015).

[59] A.-M. Schreyer, D. Sahoo, O. J. H. Williams, and A. J. Smits, Experimental investigation of two hypersonic shock/turbulent boundary-layer interactions, AIAA J. **56**, 4830 (2018).

[60] L. Cortelezzi and A. R. Karagozian, On the formation of the counter-rotating vortex pair in transverse jets, J. Fluid Mech. **446**, 347 (2001).

[61] G. S. Settles, T. J. Fitzpatrick, and S. M. Bogdonoff, Detailed study of attached and separated compression corner flowfields in high reynolds number supersonic flow, AIAA J. **17**, 579 (1979).

[62] M. S. Loginov, N. A. Adams, and A. A. Zheltovodov, Large-eddy simulation of shock-wave/turbulent-boundary-layer interaction, J. Fluid Mech. **565**, 135 (2006).

[63] M. Grilli, S. Hickel, and N. A. Adams, Large-eddy simulation of a supersonic turbulent boundary layer over a compression–expansion ramp, Int. J. Heat Fluid Flow **42**, 79 (2013).